

1 **Microphysical characteristics of precipitation within** 2 **convective overshooting over East China observed by** 3 **GPM DPR and ERA5**

4 Nan Sun¹, Gaopeng Lu¹, Yunfei Fu¹

5 ¹School of Earth and Space Sciences, University of Science and Technology of China, Hefei, 230026,
6 China

7 *Corresponding to:* Yunfei Fu, fyf@ustc.edu.cn

8 **Abstract.** We examine the geographical distribution and microphysical three-dimensional structure of
9 convective overshooting over East China by matching Global Precipitation Measurement
10 Dual-frequency Precipitation Radar instrument (GPM DPR) with European Centre for Medium-Range
11 Weather Forecasts 5th Reanalysis (ERA5). Convective overshooting mainly occur over Northeast China
12 (NC) and northern Middle and East China (MEC) and its frequency varies from 4×10^{-4} to 5.4×10^{-3} .
13 Radar reflectivity of convective overshooting over NC accounts for a higher proportion below the
14 freezing level, while MEC and South China (SC) account for a higher proportion above the freezing level,
15 indicating stronger upward motion and more ice crystal particles. The microphysical processes within
16 convective overshooting are unique, leading to various properties of the droplets in precipitation.
17 Droplets of convective overshooting are large, but sparse, with an effective droplet radius of nearly 2.5
18 mm below 10 km, which is about twice that of non-overshooting precipitation. Findings of this study
19 may have important implications for the microphysical evolution associated with convective
20 overshooting, and provide more accurate precipitation microphysical parameters as input for model
21 simulations.

23 **1 Introduction**

24 Convective overshooting provides a rapid transport mechanism that can irreversibly transport water
25 vapor and chemical constituents from lower troposphere to the upper troposphere and lower stratosphere
26 (UTLS) by mixing them with environmental air (Fueglistaler et al., 2004; Frey et al., 2015), which has a
27 direct impact on radiation balance and global climate change (Solomon et al., 2010). As one of the main
28 sources of ozone destroying OH hydroxyl radicals, stratospheric water vapor can help to destroy ozone,
29 which has potential effects on radiative forcing (Anderson et al., 2012). Water vapor enters the
30 stratosphere mainly through the tropical tropopause layer. Several studies show that tropical convective
31 overshooting has a net dehydrating effect on the stratospheric humidity (Danielsen, 1993; Sherwood and
32 Dessler, 2001), while modeling and observational studies have universally show tropical convective
33 overshooting hydrating the stratosphere (Chaboureau et al. 2007; Jensen et al. 2007; de Reus et al. 2009;
34 Avery et al. 2017) because of the injection of ice mass into the stratosphere (Grosvenor et al., 2007; Corti
35 et al., 2008; Chemel et al., 2009; Khaykin et al., 2009). In midlatitude, observations and model
36 simulations show that deep convective overshooting is also an important source for the lower
37 stratospheric water vapor (Liu and Liu, 2016; Smith et al., 2017; Liu et al., 2020; Werner et al., 2020;
38 Wang et al., 2023). Wang et al. (2023) use a high-resolution numerical model to study convective
39 overshooting moistening in the midlatitude lower stratosphere and results show that convective water
40 vapor plumes above 380-K temperature are stable in the stratosphere, while that closer to the
41 tropopause and cloud tops are less stable. In addition to these impacts on water vapor, the effects of
42 convective overshooting on the temperature of the UTLS have also attracted much attention (Sherwood
43 et al., 2003; Chae et al., 2011; Biondi et al., 2012). ~~In addition to UTLS composition effects, convective
44 overshooting is often associated with severe and hazardous weather (e.g., heavy rain, hail, tornadoes, and
45 strong winds) at the Earth's surface, with important social and economic impacts (Line et al., 2016;
46 Bedka et al., 2018; Marion et al., 2019).~~ Given these potentially significant impacts, it is of high
47 importance to understand the characteristics of convective overshooting, which have attracted
48 considerable attention in recent years (Johnston et al., 2018; Muhsin et al., 2018).

49 Perhaps one of the most poorly understood features of convective overshooting is the microphysical
50 structure of precipitation, such as particle size, concentration, phase state and other parameters.
51 Understanding the microphysical characteristics of convective overshooting is helpful to clarify the

带格式的：字体颜色：绿色

52 efficiency of water vapor transport to the lower stratosphere by convective overshooting. ~~In addition,~~
53 And the microphysical processes within convective overshooting are closely related to storm dynamics
54 and thermodynamics through latent heat, and the quantitative description of microphysical
55 characteristics is helpful to improve the accuracy of model simulation parameters (Homeyer and
56 Kumjian, 2015). In addition, thunderstorms with overshooting tops are closely associated with
57 hazardous weather at the Earth's surface, such as heavy rainfall, large hail, damaging winds and
58 tornadoes (Reynolds, 1980; Negri and Adler, 1981; Fujita 1989; Kellenbenz et al., 2007; Brunner et al.,
59 2007; Setvák et al. 2010; Dworak et al. 2012; Line et al., 2016; Bedka et al., 2018; Marion et al., 2019),
60 indicating the application of overshooting detections for severe weather warnings (McCann 1983;
61 Bedka, 2011; Homeyer and Kumjian, 2015). Bedka (2011) have studied relationship between
62 overshooting cloud tops with severe weather over Europe and results show that an overshooting was
63 found near 47% of the confirmed severe weather events. Specifically, overshooting top-severe weather
64 relationship is strong for large hail (53%) and severe wind (52%) but relatively weak for tornado events
65 (14%). Dworak et al. (2012) show that severe weather was often associated with overshooting
66 detections during warm season (April-September). Furthermore, convective overshooting generates
67 gravity waves, and gravity wave breaking generates turbulence, which is of fundamental importance in
68 the generation of small-scale motions that influence aircraft (Lane and Sharman, 2006). Tens of
69 commercial airline passengers are injured each year over the continental United States during
70 turbulence-related aviation incidents (Lane et al., 2003). Cloud-to-ground lightning is also found to
71 occur frequently near convective overshooting region, which is also a threat to aviation safety (Bedka,
72 2011). In summary, hazardous weather accompanied by convective overshooting have serious harm to
73 social economy and human production and life. Quantitative study of the precipitation structure of
74 convective overshooting can help figure the relationship between convective overshooting and severe
75 weather like heavy rainfall out, providing a predictor for severe weather warning and ensuring aviation
76 safety. Liu et al. (2012) studied the climatological characteristics of convective overshooting and found
77 convective overshooting show remarkable regionality and seasonal variations.- Homeyer and Kumjian
78 (2015) observed the radar reflectivity characteristics of convective overshooting from the analysis of the
79 polarimetric radar observations. Although the above studies have explored the characteristics of some
80 precipitation parameters within convective overshooting, we still lack the understanding of more

81 precipitation microphysical parameters and more detailed microphysical processes within convective
82 overshooting due to the limitations of observation methods.

83 To fully study the microphysical characteristics of convective overshooting, accurate methods of
84 detecting the frequency and long-term distribution of convective overshooting are required. The
85 traditional way for detecting convective overshooting from satellite is to find pixels in infrared imagery
86 with brightness temperatures colder than a given temperature threshold (Machado et al. 1998; Rossow
87 and Pearl 2007). Gettelman et al. (2002) have studied the cloud regions colder than the tropopause
88 temperature on infrared images and found that the frequency of tropical convective overshooting is about
89 0.5%. However, it is impossible to guarantee that the low value of infrared brightness temperature
90 represents clouds penetrating the tropopause rather than cirrus or cloud anvil in the upper air due to the
91 lack of vertical structure information of convection. Also, overshoots mix with relatively warm
92 stratosphere air such that cold pixels are often diminished and not a reliable means to identify overshooting.
93 With the launch of Precipitation Radar aboard Tropical Rainfall Measuring Mission (TRMM),
94 three-dimensional structure information of precipitation within the convective overshooting can be
95 provided (Alcala and Dessler, 2002; Liu and Zipser, 2005) and a new method for detecting the
96 convective overshooting is proposed that is to find pixels with rain top height higher than tropopause
97 height (Xian and Fu, 2015; Sun et al., 2021), which improves the accuracy of detecting convective
98 overshooting. Still, TRMM PR can't provide the precipitation microphysical information, which limits
99 our study on the internal microphysical structure within convective overshooting. Besides, TRMM PR
100 can underestimate the height of convective overshooting because of only sensitive to large precipitation
101 particles (sensitivity at ~17 dBZ) (Hani and Zheng, 2014).

102 As the continuation of TRMM PR, Global Precipitation Measurement (GPM) carrying the first
103 Dual-frequency Precipitation Radar (DPR) launched in February 2014. GPM DPR include two bands of
104 precipitation radar, which provides excellent opportunities for studying the microphysical structure of
105 precipitation (Sun et al., 2022a). Liu et al. (2016, 2020) have used GPM KuPR and ERA-Interim
106 6-hourly dataset to study climatology and detection of convective overshooting. However, the above
107 studies only use the KuPR data and mainly focus on the geographical distribution; the vertical and
108 microphysical processes-precipitation structure of convective overshooting remain unknown. _

109 ~~Another difficulty in convective overshooting detection is to obtain tropopause height data with high~~
110 ~~spatial and temporal resolution. On the one hand, the determination of the tropopause is still under debate.~~

111 ~~At present, the following four definitions of the tropopause are widely adopted throughout the world:~~
112 ~~Cold point tropopause, thermal tropopause, dynamic tropopause and ozone tropopause. Cold point~~
113 ~~tropopause is only physically meaningful in the latitude zone 10°S–10°N near the equator (Highwood~~
114 ~~and Hoskins, 1998; Rodriguez-Franco and Cuevas, 2013). Dynamic tropopause is based on the differing~~
115 ~~values of potential vorticity in the troposphere and stratosphere, which applies to extratropical areas~~
116 ~~(Danielsen et al., 1987; Holton et al., 1995). Ozone tropopause is defined based on the ozone sounding~~
117 ~~profiles, whose disadvantage is that the choice of ozone mixing ratio thresholds varies with region and~~
118 ~~season (Bethan et al., 1996; Zahn et al., 2004). Therefore, this paper uses the thermal tropopause, which~~
119 ~~is defined by the World Meteorological Organization (WMO) (WMO, 1957). The thermal tropopause is~~
120 ~~based on the temperature lapse rate, also known as lapse rate tropopause. The accurate calculation of the~~
121 ~~tropopause height based on this definition, on the other hand, depends on the temperature profile data~~
122 ~~with high spatial and temporal resolution. The latest generation of reanalysis data ERA5 provides hourly~~
123 ~~estimates of a large number of atmospheric, land and oceanic climate variables, which has attracted much~~
124 ~~attention due to its much higher spatial and temporal resolution than its predecessor ERA-Interim,~~
125 ~~especially in the upper troposphere and lower stratosphere (Hoffmann et al. 2019). Sun et al. (2022b)~~
126 ~~verified the accuracy for the tropopause height calculated from temperature profiles of ERA5 by~~
127 ~~comparing ERA5 with other popular datasets.~~

128 East China is a densely populated area, an economic concentration area and an important food
129 producing area in China. East China is located in the East Asian monsoon region, with unique climate
130 characteristics. The precipitation of East China in summer is affected–Affected by the circulation
131 anomalies of the East Asian tropical and subtropical monsoon and their interactions, extreme
132 precipitation events occur frequently over East China.–The precipitation anomalies not only have an
133 important impact on industrial and agricultural production, social infrastructure construction, but also
134 threaten the safety of human life and property.– Many scholars have studied the characteristics of
135 precipitation in East China (Zhang et al., 2018; Xu, 2020), but few have studied the characteristics of
136 convective overshooting and its internal precipitation microphysical structure over East China, which
137 can not only help the flood prevention work in summer over East China, but also ensure social
138 economic development to a certain extent. In addition, there are thousands of airlines over East China,
139 carrying hundreds of millions of passengers every year. In view of the impact of convective
140 overshooting on social economic and aviation safety, it's necessary to conduct relevant research on

带格式的: 字体: (中文) +中文正文 (宋体), (中文) 中文(中国)

141 | East China. –The purpose of this study is to–_examine the microphysical characteristics of convective
142 overshooting over East China by matching the precipitation data from GPM DPR and meteorological
143 parameters from ERA5. We will focus on the vertical structure of precipitation within convective
144 overshooting and further explore its microphysical structure feature of precipitation.

145 2 Data and method

146 2.1 DPR-based precipitation dataset

147 GPM DPR include KuPR (Ku band, 13.6 GHz) and KaPR (Ka band, 35.5 GHz), two bands of
148 precipitation radar. KuPR is similar to TRMM PR and has a longer wavelength, which is better at
149 detecting heavy precipitation (the minimum detected precipitation is about 0.5 mm/h). However, KaPR
150 has a shorter wavelength, which is more sensitive to weak precipitation (the minimum detected
151 precipitation is about 0.2 mm/h). Based on the different echo characteristics of Ku band and Ka band, the
152 dual channel inversion algorithm can be used to retrieve Droplet Size Distribution (DSD). Here we use
153 the precipitation datasets are provided by the GPM level 2 product 2ADPR in version 6. The horizontal
154 resolution is 5 km and the vertical resolution is 125m. The precipitation microphysical parameters
155 provided by GPM 2ADPR include droplet concentration ($dB N_0$) and effective radius (D_0).

156 2.2 ERA5-based meteorological dataset

157 The meteorological data are from ERA5 reanalysis product, whose name is “ERA5 hourly data on
158 pressure levels from 1940 to present”. . And the following parameters are used in this paper: temperature,
159 specific humidity, vertical velocity, ~~ozone mass mixing ratio~~, U-component of wind, and V-component
160 of wind. The time resolution is 1 h and the horizontal resolution is $0.25^\circ \times 0.25^\circ$. Vertical coverage is
161 1000 hPa to 1hPa and vertical resolution is 37 pressure levels (1000, 975, 950, 925, 900, 875, 850, 825,
162 800, 775, 750, 700, 650, 600, 550, 500, 450, 400, 350, 300, 250, 225, 200, 175, 150, 125, 100, 70, 50,
163 30, 20, 10, 7, 5, 3, 2, 1 hPa).

164 2.3 Detection method of convective overshooting

165 | Convective overshooting is defined to occur where the storm top height is above the real-time
166 tropopause height in a precipitation pixel. Obtaining correct tropopause height data with high spatial
167 and temporal resolution is the most important and difficult step in convective overshooting detection.

168 On the one hand, the determination of the tropopause is still under debate. At present, the following four
169 definitions of the tropopause are widely adopted throughout the world: Cold point tropopause, thermal
170 tropopause, dynamic tropopause and ozone tropopause. Cold point tropopause is only physically
171 meaningful in the latitude zone 10°S-10°N near the equator (Highwood and Hoskins, 1998;
172 Rodriguez-Franco and Cuevas, 2013). Dynamic tropopause is based on the differing values of potential
173 vorticity in the troposphere and stratosphere, which applies to extratropical areas (Danielsen et al.,
174 1987; Holton et al., 1995). Ozone tropopause is defined based on the ozone sounding profiles, whose
175 disadvantage is that the choice of ozone mixing ratio thresholds varies with region and season (Bethan
176 et al., 1996; Zahn et al., 2004). Therefore, this paper uses the thermal tropopause, which is defined by
177 the World Meteorological Organization (WMO) (WMO, 1957). The thermal tropopause is based on the
178 temperature lapse rate, also known as lapse-rate tropopause. The accurate calculation of the tropopause
179 height based on this definition, on the other hand, depends on the temperature profile data with high
180 spatial and temporal resolution. The latest generation of reanalysis data ERA5 provides hourly estimates
181 of a large number of atmospheric, land and oceanic climate variables, which has attracted much attention
182 due to its much higher spatial and temporal resolution than its predecessor ERA-Interim, especially in the
183 upper troposphere and lower stratosphere (Hoffmann et al. 2019). Sun et al. (2022b) verified the
184 accuracy for the tropopause height calculated from temperature profiles of ERA5 by comparing ERA5
185 with other popular datasets. Based on the above analysis, the process of convective overshooting
186 detection is shown as follows.

187 Firstly, match each pixel of GPM DPR detection with ERA5 grid data by using the principle of the
188 nearest method. The marching time between GPM and ERA5 is 1 h, and the matching range is $0.25^\circ \times$
189 0.25° . Storm top height is obtained from the GPM DPR. ~~Convective overshooting is defined to occur~~
190 ~~where the storm top height is above the real-time tropopause height in a precipitation pixel.~~
191 ~~Another difficulty in convective overshooting detection is to obtain tropopause height data with high~~
192 ~~spatial and temporal resolution. On the one hand, the determination of the tropopause is still under debate.~~
193 ~~At present, the following four definitions of the tropopause are widely adopted throughout the world:~~
194 ~~Cold point tropopause, thermal tropopause, dynamic tropopause and ozone tropopause. Cold point~~
195 ~~tropopause is only physically meaningful in the latitude zone 10°S-10°N near the equator (Highwood~~
196 ~~and Hoskins, 1998; Rodriguez-Franco and Cuevas, 2013). Dynamic tropopause is based on the differing~~
197 ~~values of potential vorticity in the troposphere and stratosphere, which applies to extratropical areas~~

198 (Danielsen et al., 1987; Holton et al., 1995). Ozone tropopause is defined based on the ozone sounding
199 profiles, whose disadvantage is that the choice of ozone mixing ratio thresholds varies with region and
200 season (Bethan et al., 1996; Zahn et al., 2004). Therefore, this paper uses the thermal tropopause, which
201 is defined by the World Meteorological Organization (WMO) (WMO, 1957). The thermal tropopause is
202 based on the temperature lapse rate, also known as lapse rate tropopause. The accurate calculation of the
203 tropopause height based on this definition, on the other hand, depends on the temperature profile data
204 with high spatial and temporal resolution. The latest generation of reanalysis data ERA5 provides hourly
205 estimates of a large number of atmospheric, land and oceanic climate variables, which has attracted much
206 attention due to its much higher spatial and temporal resolution than its predecessor ERA Interim
207 especially in the upper troposphere and lower stratosphere (Hoffmann et al. 2019). Sun et al. (2022b)
208 verified the accuracy for the tropopause height calculated from temperature profiles of ERA5 by
209 comparing ERA5 with other popular datasets.

210 Secondly, Real-time tropopause height is calculated from the temperature profiles from ERA5
211 according to the definition from the World Meteorological Organization (WMO, 1957). The
212 algorithmic process is shown as follows: Firstly, find X layer whose atmospheric lapse rate is 2 K km^{-1}
213 or less starting from the first layer (near the ground) of the temperature profile, and then judge whether
214 the atmospheric lapse rate does not exceed 2 K km^{-1} between the X level and all higher levels within 2
215 km, if so, the height of X layer is the tropopause height, if not, repeat the above algorithm starting from
216 the X layer until tropopause layer is found.

217 At last, convective overshooting is identified based on the storm top height and tropopause height.

218 **2.4 Study areas**

219 The study areas are marked as black boxes in Fig. 1a and only the land parts are studied because
220 characteristics of vertical structure of precipitation over land and sea are very different, and this study
221 is limited in space and focuses only on the land region. Using years of NCEP/NCAR reanalysis data,
222 Xia (2015) analyzed the climatic feature of temperature and water vapor in China and divided China into
223 different climatic zones. To have a better understanding of precipitation microphysical structure over
224 different regions of East China, we also divided East China into three climatic zones according to its
225 climatic characteristics and previous studies (Xia, 2015; Sun et al., 2022a). From north to south, they are
226 Northeast China (NC, 38° – 50° N, 118° – 130° E), Middle and East China (MEC, 26.5° – 38° N, 112° –

227 123 E), and South China (SC, 18 °-26.5 N, 108 °-123 E). For the three regions, the lower latitude areas
228 have higher surface temperature, greater temperature lapse rate and lower temperature of stratosphere.
229 Temperature profiles of same latitude are essentially same over SC and MEC, and temperature signals
230 exist meridional differences over NC. Atmospheric humidity has remarkable regional characteristics.
231 SC is wetter, with the surface relative humidity of more than 70%, while NC and MEC are drier and
232 their humidity range from 50% to 70% (Xia, 2015). The study time frame is defined as the time from
233 2014 to 2020 in summer (June, July and August)

234 **3 Results**

235 **3.1 Case studies**

236 Three cases selected from NC, MEC and SC are analyzed to lay a foundation for the subsequent
237 statistical analysis. The precipitation characteristics of the three cases are shown as Fig. 2. The Case 1
238 (C1) occurs in NC at 14:00 on July 1, 2017. Convective overshooting is observed in a total of 65 pixels
239 for C1, whose mean rain rate are 20.7 mm/h (Fig. 2a) and mean storm top height are 14.1 km (Fig. 2b).
240 The strong radar reflectivity along A1B1 occurs at 35-95km away from point A1, and the strongest echo
241 is up to 50 dBZ, appears at 0-5 km (Fig. 2c). The maximum echo height is about 15 km, 2 km higher than
242 the tropopause height. The Case 2 (C2) occurs in MEC at 13:00 on July 30, 2015. Convective
243 overshooting is observed in a total of 58 pixels for C2, and their mean rain rate are 29.7 mm/h (Fig. 2d)
244 and mean storm top height are 15.2 km (Fig. 2e). The radar echo along A2B2 is very strong and the
245 strongest echo is up to 50 dBZ, which is about 45-95 km away from point A2 (Fig. 2f). The highest echo
246 can reach to about 17 km altitude. The Case 3 (C3) occurs in SC at 17:00 on June 13, 2015. Convective
247 overshooting is observed in a total of 8 pixels for C3 and their mean rain rate are 46.3 mm/h (Fig. 2g) and
248 mean storm top height are 16.9 km (Fig. 2h). The strongest echo occurs at 60-70 km away from point A3
249 and the highest echo can reach to 17.2 km, about 0.5 km higher than the tropopause height (Fig. 2i).
250 To learn about the characteristics of the large scale circulation for these three cases, we calculate the
251 distribution of Precipitable Water Vapor (PWV), streamlines and Vertical Velocity (VV), and locations
252 of the three cases are shown as the black boxes in Fig. 3. In general, areas in which convective
253 overshooting occur have abundant PWV and strong ascending movement. In C1, The PWV of the region
254 in which convective overshooting occurs is between 50 and 55 mm, which is higher than otherwise (Fig.

255 3a). Upward motion near the convective overshooting is strong, ranging from -0.03 to -0.12 Pa/s,
256 contributing to the occurrence of convective overshooting (Fig. 3b). The PWV of C2 is more abundant
257 than C1, and the PWV of the area in which convective overshooting occurs are between 55 and 60 mm
258 (Fig. 3c). The VV near the convective overshooting is mostly between -0.09 and -0.15 Pa/s (Fig. 3d). In
259 C3, the PWV near the precipitation area and convective overshooting area are the most abundant
260 compared with C1 and C2, whose maximum can exceed 70 mm (Fig. 3e). Upward movement near the
261 precipitation area and convective overshooting area are very strong and the VV are between -0.12 and
262 -0.18 Pa/s, which provide abundant water vapor and dynamic conditions for the occurrence of
263 convective overshooting.

264 **3.2 Statistical results**

265 **3.2.1 Geographical distribution**

266 Firstly, the horizontal distribution characteristics of convective overshooting over East China are
267 analysed by designing a more accurate algorithm for convective overshooting determination. Accurate
268 determination of tropopause height is the first step of the convective overshooting determination
269 algorithm. We first analyze geographical distribution of climatological mean of the tropopause height
270 over East China calculated from ERA5, shown as Fig. 1b. In general, the tropopause height over East
271 China is between 11.6 km and 16.7 km and has an obvious zonal distribution pattern: Tropopause height
272 over SC and southern MEC (18-36 °N) is the highest and has small spatial variabilities, concentrated at
273 ~16.7 km. Over northern MEC (36-38 °N), tropopause height decreases and forms a gradient, which
274 decreases to 16 km. Tropopause height over NC is the lowest and continues to decrease in a gradient
275 pattern from south to north, decreasing to 13 km near central NC (45 °N) and 12 km near northern NC
276 (48 °N). Minimum standard deviation of tropopause height appears in SC, along with central and
277 southern MEC, lower than 0.2 km. From northern MEC to northern NC, the standard deviation first
278 increases and then decreases, reaching a maximum of more than 2 km around 42 °N, and standard
279 deviation over NC is generally above 1 km.

280 Obtaining storm top height from precipitation data is the second step of convective overshooting
281 algorithm. Fig. 4 show geographical distribution of storm top height for total precipitation, convective
282 precipitation and convective overshooting. Total precipitation represent the all pixels with rain rate
283 higher than 0 mm/h detected by GPM DPR, and those pixels whose rain type are “Convective” are

284 defined as convective precipitation. As shown, mean storm top height over East China varies from 4.5
285 km to 8.5 km, while convective storm top height is mainly distributed between 3.5 km and 9 km.
286 Convective storm top height over NC and northern MEC are the highest, with most areas exceeding 6.5
287 km and as we noted above, tropopause height in these two regions are lower (Fig. 1b), it can be inferred
288 that convective overshooting events are more likely to occur. Further analysis of the frequency of
289 convective overshooting in the following text will confirm this point. Compared with NC, convective
290 storm top height over SC and southern MEC is lower, mainly distributed below 6.5 km. Storm top height
291 of convective overshooting ranges from 10 km to 21 km (Fig. 4c), much higher than normal precipitation
292 (total and convective precipitation) and increasing gradually from north to south. Storm top heights of
293 convective overshooting over NC and northern MEC are low, distributed between 10 km and 16 km,
294 which is due to a lower tropopause height (Fig. 1b) allowing convection with lower storm top height to
295 reach the stratosphere. This lowers the mean storm top height of convective overshooting in these
296 regions, while tropopause heights over SC and southern MEC range from 16 km to 21 km (Fig. 1b),
297 allowing only strong convection to reach the stratosphere.

298 The frequency of convective overshooting is defined as the number of convective overshooting events
299 divided by the total observed sample number of GPM DPR. Statistical results indicate that the frequency
300 of the convective overshooting over East China is very low, with a magnitude of only 10^{-3} , varying
301 regionally (Fig. 5). Sample size of convective overshooting over NC is the highest, followed by MEC,
302 and SC is the lowest (Table 1). Convective overshooting over NC and northern MEC, whose frequency
303 range from 4×10^{-4} to 5.4×10^{-3} (Fig. 5), occur more frequently than SC and southern MEC, whose
304 frequency is between 2×10^{-4} and 6×10^{-4} , which is mainly because the former has a lower tropopause
305 height and it's easier for convective overshooting to occur.

306 3.2.2 Vertical structures

307 Based on the reflectivity profiles and the rain-rate profiles provided by the GPM DPR instrument, we
308 studied the vertical structure of precipitation within convective overshooting. Contoured Frequency by
309 Altitude Diagrams (CFADs) analysis of radar reflectivity can effectively indicate the three-dimensional
310 structure characteristics of precipitation, which is therefore applied in a large number of precipitation
311 studies (Yuter and Houze, 1995). Fig. 6 shows CFADs of the DPR radar reflectivity. In general, radar
312 reflectivity within convective overshooting is stronger and its storm top height is higher. And the

313 CFADs analysis also shows regional differences. Radar echo intensity of convective overshooting over
314 NC is the weakest, and the echo near surface is mainly distributed from 25 dBZ to 55 dBZ, with sharp
315 peak near 47 dBZ, while the peak of the total precipitation is around 16 dBZ. And the max radar echo top
316 within convective overshooting over NC can reach to 13.5 km, 3.3 km higher than the mean precipitation.
317 Compared with NC, radar reflectivity within convective overshooting over SC and MEC are stronger and
318 their CFADs character is more similar. Their echo top height is ~18 km, 6.5 km higher than total
319 precipitation, 4.5 km higher than NC, and their echo near surface concentrated around 30-55 dBZ, while
320 that of total precipitation is between 15 dBZ and 43 dBZ. Besides, Radar reflectivity of convective
321 overshooting over NC accounts for a higher proportion below the freezing level (Altitude where the
322 temperature is 0 °C), while MEC and SC account for a higher proportion above the freezing level, which
323 indicate that the upward motion within convective overshooting over MEC and SC are stronger and there
324 are larger.

325 Quantitative analysis of the vertical structure of precipitation within convective overshooting is one of
326 the main issues of interest to this study. Shown as Fig. 7, the rain rate profiles of convective overshooting
327 are provided, and to highlight its unique feature, rain rate profiles of total precipitation and convective
328 precipitation are also given. In general, the rain rate of convective overshooting is much higher,
329 especially below the freezing level (~5 km), 5-10 times that of normal precipitation. This indicates
330 stronger convection and a greater concentration of ice. In addition, differences between three regions are
331 obvious. Rain rate of convective overshooting over NC are about half as high as over MEC and SC,
332 which is consistent with the results of radar echo. At 1 km altitude, rain rate of convective overshooting
333 are 12 mm/h (NC), 22.5 mm/h (MEC), and 23 mm/h (SC) respectively. Below freezing level, the
334 variation of rain rate with altitude is not very obvious, and difference of rain rate between convective
335 overshooting and normal precipitation are ~8 mm over NC and ~20 mm over MEC and SC. Above
336 freezing level, rain rate of convective overshooting clearly decreases with increasing altitude, and rain
337 rates are 6mm/h (NC), 10 mm (MEC) and 6.5mm (SC) at 10 km. However, rain rates of other
338 precipitation are no more than 2 mm/h above 8 km, we therefore suggest that the strong upward flow
339 within convective overshooting brings large amounts of moisture from the lower layer to the upper layer.

340 We conduct the Probability Density Function (PDF) analysis on the Near Surface Rain Rate (NSRR)
341 within convective overshooting, and that of total and convective precipitation are also calculated, shown
342 as Fig. 8. Grade of precipitation are as follows: Light rain: <4.9 mm/12 h, Moderate rain: 5.0-14.9

343 mm/12h, Heavy rain: 15.0-29.9 mm/12h, Torrential rain: 30.0-69.9 mm/12h, Downpour: 70.0-139.9
344 mm/12h, and Heavy downpour: ≥ 140.0 mm/12h (General Administration of Quality Supervision, 2012).
345 The PDF curve of NSRR of convective overshooting is clearly different from normal precipitation, and
346 has regional differences. The peak value of PDF of convective overshooting appears at ~ 10 mm/h,
347 classified as downpour, while that of normal precipitation appears at ~ 1 mm/h, classified as moderate
348 rain, which is obviously lower than convective overshooting. And the PDF of peak value of convective
349 overshooting over NC is about 11.5%, while that over MEC and SC are about 6%. Besides, sample size
350 of convective overshooting with precipitation grade of heavy downpour account for 34.0% (NC), 46.7%
351 (MEC) and 34.8% (SC) respectively, 3-10 times than normal precipitation, which remind us to pay
352 special attention to the extreme precipitation events caused by convective overshooting that may cause
353 harm to our production and life.

354 3.2.3 Microphysical features

355 GPM center provides particle spectrum from dual-frequency radar. Based on the DSD profiles from
356 2ADPR, we further investigate the microphysical structures of convective overshooting. The Liquid
357 Water Path (LWP) and Ice Water Path (IWP) show the overall water content in the atmospheric column,
358 which is closely associated with microphysical processes within convective overshooting. To quantify
359 the characteristics of LWP and IWP within convective overshooting, the PDF of LWP and IWP of
360 convective overshooting are shown as Fig. 9, and that of convective and total precipitation are also
361 shown for comparison. The LWP and IWP within convective overshooting are the highest, with high
362 value of PDF mainly distributed around 1000 g/m^3 and 5000 g/m^3 respectively, much higher than that of
363 normal precipitation, which are around 100 g/m^3 and 300 g/m^3 , indicating sufficient water vapor inside
364 convective overshooting. And differences of IWP between convective overshooting and normal
365 precipitation are bigger than LWP, suggesting that differences of water vapor above freezing level
366 between them is greater and convective overshooting brings water vapor from bottom of the troposphere
367 to higher layers. Besides, differences of LWP and IWP between three regions are also worth noting: The
368 LWP and IWP over MEC and SC are more similar and higher than NC. Especially, LWP over MEC has
369 a bimodal structure with peaks of 630 and 5000 g/m^3 , which are consistent with the bimodal structure of
370 NSRR PDF curve in Fig. 8. Analysis above in Fig. 1b shows that tropopause height over northern MEC
371 is lower than southern MEC, making it easier for convective overshooting to occur over northern MEC.

372 This indicates that there are two types of convective overshooting events over MEC, weak events with
373 lower storm top height and strong events with higher storm top height, which correspond to the two
374 peaks of LWP PDF curve respectively.

375 We further use DSD parameter profiles, including the effective radius (D_0) and droplet concentration
376 (dBN_0) profiles, to analyze the microphysical characteristics within convective overshooting, shown as
377 Fig. 10. Results show that the microphysical processes within convective overshooting are unique,
378 leading to various properties of the droplets in precipitation. Droplets of convective overshooting are
379 large, but sparse. Influenced by strong updrafts, precipitation particles within convective overshooting
380 continuously collide and grow large enough to fall, therefore, the effective radius of droplets are big,
381 below 10 km altitude, almost exceeding 2.5 mm, which is about twice than that of normal precipitation.
382 However, the droplet concentration within convective overshooting is relatively lower. Differences of
383 microphysical structure between three regions are also worth noting. Convective overshooting events
384 over NC have large, but sparse droplets, while that over SC have small, but dense droplets, and the
385 effective radius and concentration of droplets over MEC are between NC and SC, which is speculated
386 that it's related to the differences of aerosol content and types over three regions. Specifically, at 1 km
387 altitude, the effective radius of droplets over NC is the largest (2.87 mm), followed by MEC (2.7 mm),
388 and SC is the lowest (2.5 mm). As altitude increases, the effective radius of droplets first increase and
389 then decrease, with maximum of 2.93 mm over NC at 2.5 km and sharp peak over MEC (2.85 mm) and
390 SC (2.76 mm) near freezing level, about twice than normal precipitation. The effective radius of droplets
391 for convective overshooting over NC and MEC are lower than 2.5 mm above 10 km and 12 km
392 respectively. It's worth noting that the effective radius of droplets for convective overshooting over SC
393 show an increasing trend above 8 km altitude, which are similar to convective precipitation, and their
394 effective radius of droplets over three regions also show an increasing trend from 9 km to 13 km, which
395 may be related to the strong upward motion inside. When the upward motion is strong, ice particles must
396 grow large enough to fall (Langmuir, 1948). Droplet concentration basically decreases with altitude, and
397 that within convective overshooting is obviously lower than normal precipitation and NC is the lowest,
398 while MEC and SC are higher and similar. Droplet concentration within convective overshooting near
399 ground is the highest, with NC (25.4), MEC (28) and SC (28), while that of normal precipitation is
400 mainly distributed between 32 and 35.

401 **4 Summary and conclusions**

402 The microphysical characteristics of convective overshooting are essential but poorly understood due to
403 the difficulty in accurately detecting the convective overshooting and obtaining microphysical
404 parameters during severe weather events. Based on the microphysical precipitation data from GPM DPR
405 and the meteorological data from ERA5 data, we designed a more accurate algorithm for convective
406 overshooting determination and examine the particle size, concentration, phase state and other
407 parameters of the convective overshooting over East China. The main conclusions are:

408 Firstly, the horizontal distribution characteristics of convective overshooting over East China are
409 analysed by designing a more accurate algorithm for convective overshooting determination. Statistical
410 results indicate that the frequency of the convective overshooting over East China is very low, with a
411 magnitude of only 10^{-3} , with large regional differences. Convective overshooting events occur more
412 frequently over NC and northern MEC, than SC and southern MEC, mainly because of the lower
413 tropopause height of the former and the different underlying surfaces. The mean convective overshooting
414 storm top height mostly ranges from 10 km to 21 km and has obvious regional distribution differences,
415 and convective overshooting storm top height over NC is 5-6 km higher than SC.

416 Based on the reflectivity profiles and the rain-rate profiles provided by the GPM DPR instrument, we
417 studied the vertical structure of precipitation within convective overshooting. The CFADs analysis of the
418 radar reflectivity shows that radar reflectivity within convective overshooting is stronger and its storm
419 top height is higher. The CFADs analysis also shows regional differences. Radar reflectivity of
420 convective overshooting over NC accounts for a higher proportion below the freezing level, while MEC
421 and SC account for a higher proportion above the freezing level, which indicate that the upward motion
422 within convective overshooting over MEC and SC are stronger and there are more ice crystal particles.
423 Rain rate results also show that rain rate within convective overshooting is higher, 5-10 times than that of
424 normal precipitation. Especially, sample number of strong precipitation with grade of precipitation of
425 heavy downpour accounts for 34.0% (NC), 46.7% (MEC), and 34.8% (SC), which remind us to pay
426 special attention to the extreme precipitation events caused by convective overshooting.

427 GPM center provides particle spectrum from dual-frequency radar. Based on the DSD profiles from
428 2ADPR, we further investigated the microphysical structures of convective overshooting. Statistical
429 results show that convective overshooting has unique microphysical characteristics compared with

430 normal precipitation, with obvious regional differences. The LWP and IWP within convective
431 overshooting are abundant, with high values of PDF distributed around 1000 g/m^3 and 5000 g/m^3
432 respectively. Moreover, influenced by strong updrafts, precipitation particles within convective
433 overshooting continuously collide and grow large enough to fall, therefore, the effective radius is big,
434 below 10 km altitude, almost exceeding 2.5 mm, which is about twice than that of normal precipitation.
435 However, the droplet concentration within convective overshooting is relatively lower. Differences of
436 microphysical structure between three regions are also worth noting. The effective radius of droplet over
437 NC is slightly bigger than MEC and SC, while the droplet concentration is lower, which is speculated
438 that it's related to the differences of aerosol content and types over three regions.

439 Quantitative study of the internal microphysical characteristics within convective overshooting has not
440 been documented previously. Findings of this study may have important implications for the
441 microphysical evolution associated with convective overshooting, and provide more accurate
442 precipitation microphysical parameters as the input of the model simulation. This study is the
443 continuation of the previous research (Sun et al., 2021). In the future, we will further explore the impact
444 of aerosol on the internal microphysical characteristics within convective overshooting, and more
445 microphysical parameters with higher spatiotemporal resolution are expected to provide more detailed
446 features.

447 **Data availability.** ERA5 data are taken from
448 <https://www.ecmwf.int/en/forecasts/datasets/reanalysis-datasets/era5>. GPM DPR data are archived at
449 <https://gpm.nasa.gov/data/directory>.

450 **Acknowledgements.** This work was funded by the National Natural Science Foundation of China
451 Project (Grant No. 42230612) and the fellowship of China Postdoctoral Science Foundation (Grant
452 Numbers: 2022M723011).

453 **Author contributions.** Sun N., Lu G.P., and Fu Y.F. framed up this study. All the authors discussed the
454 concepts. Sun N. conducted the data analyses. Sun N. drafted the manuscript and all authors edited the
455 manuscript.

456 **Competing interests.** The authors declare no competing interests.

457 **References**

458 Anderson, J. G., Wilmouth, D. M., Smith, J. B. and Sayres, D. S.: UV dosage levels in summer:
459 Increased risk of ozone loss from convectively injected water vapor, *Science*, 337, 835-839,
460 <https://doi.org/10.1126/science.1222978>, 2012.

461 Avery, M. A., Davis, S. M., Rosenlof, K. H., Ye, H. and Dessler, A. E.: Large anomalies in lower
462 stratospheric water vapour and ice during the 2015–2016 El Niño, *Nature Geoscience*, 10, 405-409,
463 <https://doi.org/10.1038/ngeo2961>, 2017.

464 Alcala, C. M. and Dessler, A. E.: Observations of deep convection in the tropics using the Tropical
465 Rainfall Measuring Mission (TRMM) precipitation radar, *Journal of Geophysical Research:*
466 *Atmospheres*, 107, 4792, <https://doi.org/10.1029/2002JD002457>, 2002.

467 Biondi, R., Randel, W. J., Ho, S. P., Neubert, T. and Syndergaard, S.: Thermal structure of intense
468 convective clouds derived from GPS radio occultations, *Atmospheric Chemistry and Physics*, 12,
469 5309-5318, <https://doi.org/10.5194/acp-12-5309-2012>, 2012.

470 Bedka, K., Murillo, E. M., Homeyer, C. R., Scarino, B. and Mersiovsky, H.: The above-anvil cirrus
471 plume: An important severe weather indicator in visible and infrared satellite imagery, *Weather and*
472 *Forecasting*, 33, 1159-1181, <https://doi.org/10.1175/WAF-D-18-0040.1>, 2018.

473 Bethan, S., Vaughan, G., and Reid, S. J.: A comparison of ozone and thermal tropopause heights and the
474 impact of tropopause definition on quantifying the ozone content of the troposphere, *Quarterly*

475 Journal of the Royal Meteorological Society, 122(532), 929-944,
476 <https://doi.org/10.1002/qj.49712253207>, 1996.

477 [Brunner, J. C., Ackerman, S. A., Bachmeier, A. S. and Rabin, R. M.: A quantitative analysis of the](#)
478 [enhanced-V feature in relation to severe weather, *Weather and Forecasting*, 22, 853-872,](#)
479 <https://doi.org/10.1175/WAF1022.1>, 2007.

480 [Bedka, K. M.: Overshooting cloud top detections using MSG SEVIRI Infrared brightness temperatures](#)
481 [and their relationship to severe weather over Europe, *Atmospheric Research*, 99, 175-189,](#)
482 <https://doi.org/10.1016/j.atmosres.2010.10.001>, 2011.

483 Chaboureaud, J. P., Cammas, J. P., Duron, J., Mascart, P. J., Sitnikov, N. M. and Voessing, H. J.: A
484 numerical study of tropical cross-tropopause transport by convective overshoots, *Atmospheric*
485 *Chemistry and Physics*, 7, 1731-1740, <https://doi.org/10.5194/acp-7-1731-2007>, 2007.

486 Corti, T., Luo, B. P. and De Reus, M. et al.: Unprecedented evidence for deep convection hydrating the
487 tropical stratosphere, *Geophysical Research Letters*, 35, L10810,
488 <https://doi.org/10.1029/2008GL033641>, 2008.

489 Chemel, C., Russo, M. R., Pyle, J. A., Sokhi, R. S. and Schiller, C.: Quantifying the imprint of a severe
490 hector thunderstorm during ACTIVE/SCOUT-O3 onto the water content in the upper
491 troposphere/lower stratosphere, *Monthly weather review*, 137, 2493-2514,
492 <https://doi.org/10.1175/2008MWR2666.1>, 2009.

493 Chae, J. H., Wu, D. L., Read, W. G. and Sherwood, S. C.: The role of tropical deep convective clouds on
494 temperature, water vapor, and dehydration in the tropical tropopause layer (TTL), *Atmospheric*
495 *Chemistry and Physics*, 11, 3811-3821, <https://doi.org/10.5194/acp-11-3811-2011>, 2011.

496 Danielsen, E. F.: In situ evidence of rapid, vertical, irreversible transport of lower tropospheric air into
497 the lower tropical stratosphere by convective cloud turrets and by larger - scale upwelling in tropical
498 cyclones, *Journal of Geophysical Research: Atmospheres*, 98, 8665-8681,
499 <https://doi.org/10.1029/92JD02954>, 1993.

500 De Reus, M., Borrmann, S. and Bansemmer, A. et al: Evidence for ice particles in the tropical stratosphere
501 from in-situ measurements, *Atmospheric Chemistry and Physics*, 9, 6775-6792,
502 <https://doi.org/10.5194/acp-9-6775-2009>, 2009.

503 Danielsen, E. F., Hipskind, R. S. and Gaines, S. E. et al.: Three-dimensional analysis of potential
504 vorticity associated with tropopause folds and observed variations of ozone and carbon monoxide,

505 Journal of Geophysical Research: Atmospheres, 92(D2), 2103-2111,
506 <https://doi.org/10.1029/JD092iD02p02103>, 1987.

507 [Dworak, R., Bedka, K., Brunner, J. and Feltz, W.: Comparison between GOES-12 overshooting-top](#)
508 [detections, WSR-88D radar reflectivity, and severe storm reports, Weather and Forecasting, 27,](#)
509 [684-699, <https://doi.org/10.1175/WAF-D-11-00070.1>, 2012.](#)

带格式的: 字体: (中文) +中文正
文 (宋体), (中文) 中文 (中国)

510 Fueglistaler, S., Wernli, H. and Peter, T.: Tropical troposphere - to - stratosphere transport inferred from
511 trajectory calculations, Journal of Geophysical Research: Atmospheres, 109, D03108,
512 <https://doi.org/10.1029/2003JD004069>, 2004.

513 [Fujita, T. T.: The Teton-Yellowstone tornado of 21 July 1987, Monthly Weather Review, 117,](#)
514 [1913-1940, \[https://doi.org/10.1175/1520-0493\\(1989\\)117<1913:TTYTOJ>2.0.CO;2\]\(https://doi.org/10.1175/1520-0493\(1989\)117<1913:TTYTOJ>2.0.CO;2\), 1989.](#)

带格式的: 字体: (中文) +中文正
文 (宋体), (中文) 中文 (中国)

515 Frey, W., Schofield, R. and Hoor, P. et al.: The impact of overshooting deep convection on local
516 transport and mixing in the tropical upper troposphere/lower stratosphere (UTLS), Atmospheric
517 Chemistry and Physics, 15, 6467-6486, <https://doi.org/10.5194/acp-15-6467-2015>, 2015.

518 General Administration of Quality Supervision, Inspection and Quarantine of the People's Republic of
519 China: Standardization Administration of the People's Republic of China, GB/T 28592—2012 Grade
520 of precipitation, Standards Press of China, 2012.

521 Grosvenor, D. P., Choularton, T. W., Coe, H. and Held, G.: A study of the effect of overshooting deep
522 convection on the water content of the TTL and lower stratosphere from Cloud Resolving Model
523 simulations, Atmospheric Chemistry and Physics, 7, 4977-5002,
524 <https://doi.org/10.5194/acp-7-4977-2007>, 2007.

525 Gettelman, A., Salby, M. L. and Sassi, F.: Distribution and influence of convection in the tropical
526 tropopause region, Journal of Geophysical Research: Atmospheres, 107, 4080,
527 <https://doi.org/10.1029/2001JD001048>, 2002.

528 Homeyer, C. R. and Kumjian, M. R.: Microphysical characteristics of overshooting convection from
529 polarimetric radar observations, Journal of the Atmospheric Sciences, 72, 870-891,
530 <https://doi.org/10.1175/JAS-D-13-0388.1>, 2015.

531 Hoffmann, L., Günther, G. and Li, D. et al.: From ERA-Interim to ERA5: the considerable impact of
532 ECMWF's next-generation reanalysis on Lagrangian transport simulations, Atmospheric Chemistry
533 and Physics, 19, 3097-3124, <https://doi.org/10.5194/acp-19-3097-2019>, 2019.

534 Highwood, E. J. and Hoskins, B. J.: The tropical tropopause, Quarterly Journal of the Royal
535 Meteorological Society, 124, 1579-1604, <https://doi.org/10.1002/qj.49712454911>, 1998.

536 Holton, J. R., Haynes, P. H. and McIntyre, M. E. et al.: Stratosphere-troposphere exchange. Reviews of
537 geophysics, 33(4), 403-439, <https://doi.org/10.1029/95RG02097>, 1995.

538 Jensen, E. J., Ackerman, A. S. and Smith, J. A.: Can overshooting convection dehydrate the tropical
539 tropopause layer?, Journal of Geophysical Research: Atmospheres, 112, D11209,
540 <https://doi.org/10.1029/2006JD007943>, 2007.

541 Johnston, B. R., Xie, F. and Liu, C.: The effects of deep convection on regional temperature structure in
542 the tropical upper troposphere and lower stratosphere, Journal of Geophysical Research:
543 Atmospheres, 123, 1585-1603, <https://doi.org/10.1002/2017JD027120>, 2018.

544 Khaykin, S., Pommereau, J. P. and Korshunov, L. et al.: Hydration of the lower stratosphere by ice
545 crystal geysers over land convective systems, Atmospheric Chemistry and Physics, 9, 2275-2287,
546 <https://doi.org/10.5194/acp-9-2275-2009>.

547 [Kellenbenz, D. J., Grafenauer, T. J. and Davies, J. M.: The North Dakota tornadic supercells of 18 July](#)
548 [2004: Issues concerning high LCL heights and evapotranspiration, Weather and forecasting, 22,](#)
549 [1200-1213, <https://doi.org/10.1175/2007WAF2006109.1>, 2007.](#)

550 Langmuir, I.: The production of rain by a chain reaction in cumulus clouds at temperatures above
551 freezing, Journal of the Atmospheric Sciences, 5(5), 175-192,
552 [https://doi.org/10.1175/1520-0469\(1948\)005<0175:TPORBA>2.0.CO;2](https://doi.org/10.1175/1520-0469(1948)005<0175:TPORBA>2.0.CO;2), 1948.

553 [Lane, T. P. and Sharman, R. D.: Gravity wave breaking, secondary wave generation, and mixing above](#)
554 [deep convection in a three - dimensional cloud model, Geophysical Research Letters, 33,](#)
555 [<https://doi.org/10.1029/2006GL027988>, 2006.](#)

556 [Lane, T. P., Sharman, R. D., Clark, T. L. and Hsu, H. M.: An investigation of turbulence generation](#)
557 [mechanisms above deep convection, Journal of the atmospheric sciences, 60, 1297-1321,](#)
558 [\[https://doi.org/10.1175/1520-0469\\(2003\\)60<1297:AIOTGM>2.0.CO;2\]\(https://doi.org/10.1175/1520-0469\(2003\)60<1297:AIOTGM>2.0.CO;2\), 2003.](#)

559 Liu, N. and Liu, C.: Global distribution of deep convection reaching tropopause in 1 year GPM
560 observations, Journal of Geophysical Research: Atmospheres, 121, 3824-3842,
561 <https://doi.org/10.1002/2015JD024430>, 2016.

带格式的: 字体: (中文) +中文正文 (宋体), (中文) 中文(中国)

带格式的: 字体: (中文) +中文正文 (宋体), (中文) 中文(中国)

562 Liu, N., Liu, C. and Hayden, L.: Climatology and detection of overshooting convection from 4 years of
563 GPM precipitation radar and passive microwave observations, *Journal of Geophysical Research:*
564 *Atmospheres*, 125, e2019JD032003, <https://doi.org/10.1029/2019JD032003>, 2020.

565 Liu, C. and Zipser, E. J.: Global distribution of convection penetrating the tropical tropopause, *Journal of*
566 *Geophysical Research: Atmospheres*, 110, D23104, <https://doi.org/10.1029/2005JD006063>, 2005.

567 Liu, P., Wang, Y., Feng, S., Li, C. Y. and Fu, Y. F.: Climatological characteristics of overshooting
568 convective precipitation in summer and winter over the tropical and subtropical regions, *Chin. J.*
569 *Atmos. Sci.*, 36, 579-589, <https://doi.org/10.3878/j.issn.1006-9895.2011.11109>, 2012.

570 Line, W. E., Schmit, T. J., Lindsey, D. T. and Goodman, S. J.: Use of geostationary super rapid scan
571 satellite imagery by the Storm Prediction Center, *Weather and Forecasting*, 31, 483-494,
572 <https://doi.org/10.1175/WAF-D-15-0135.1>, 2016.

573 Machado, L. A. T., Rossow, W. B., Guedes, R. L. and Walker, A. W.: Life cycle variations of mesoscale
574 convective systems over the Americas, *Monthly Weather Review*, 126, 1630-1654,
575 [https://doi.org/10.1175/1520-0493\(1998\)126<1630:LCVOMC>2.0.CO;2](https://doi.org/10.1175/1520-0493(1998)126<1630:LCVOMC>2.0.CO;2), 1998.

576 Muhsin, M., Sunilkumar, S. V., Ratnam, M. V., Parameswaran, K., Murthy, B. K. and Emmanuel, M.:
577 Effect of convection on the thermal structure of the troposphere and lower stratosphere including the
578 tropical tropopause layer in the South Asian monsoon region, *Journal of Atmospheric and*
579 *Solar-Terrestrial Physics*, 169, 52-65, <https://doi.org/10.1016/j.jastp.2018.01.016>, 2018.

580 Marion, G. R., Trapp, R. J. and Nesbitt, S. W.: Using overshooting top area to discriminate potential for
581 large, intense tornadoes, *Geophysical Research Letters*, 46, 12520-12526,
582 <https://doi.org/10.1029/2019GL084099>, 2019.

583 [McCann, D. W.: The enhanced-V: A satellite observable severe storm signature. *Monthly Weather*](#)
584 [Review](#), 111, 887-894, [https://doi.org/10.1175/1520-0493\(1983\)111<0887:TEVASO>2.0.CO;2](https://doi.org/10.1175/1520-0493(1983)111<0887:TEVASO>2.0.CO;2),
585 [1983.](#)

586 [Negri, A. J. and Adler, R. F.: Relation of satellite-based thunderstorm intensity to radar-estimated](#)
587 [rainfall. *Journal of Applied Meteorology and Climatology*, 20, 288-300,](#)
588 [https://doi.org/10.1175/1520-0450\(1981\)020<0288:ROSBTI>2.0.CO;2](https://doi.org/10.1175/1520-0450(1981)020<0288:ROSBTI>2.0.CO;2), 1981.

589 [Reynolds, D. W.: Observations of damaging hailstorms from geosynchronous satellite digital](#)
590 [data. *Monthly Weather Review*, 108, 337-348,](#)
591 [https://doi.org/10.1175/1520-0493\(1980\)108<0337:OODHFG>2.0.CO;2](https://doi.org/10.1175/1520-0493(1980)108<0337:OODHFG>2.0.CO;2), 1980.

带格式的: 字体: (中文) + 中文正
文 (宋体), (中文) 中文 (中国)

592 Rodriguez - Franco, J. J. and Cuevas, E.: Characteristics of the subtropical tropopause region based on
593 long - term highly resolved sonde records over Tenerife, Journal of Geophysical Research:
594 Atmospheres, 118, 10-754, <https://doi.org/10.1002/jgrd.50839>, 2013.

595 Rossow, W. B. and Pearl, C.: 22 - year survey of tropical convection penetrating into the lower
596 stratosphere, Geophysical research letters, 34, L04803, <https://doi.org/10.1029/2006GL028635>,
597 2007.

598 [Setvák, M., Lindsey, D. T. and Novák, P. et al.: Satellite-observed cold-ring-shaped features atop deep](#)
599 [convective clouds. Atmospheric Research, 97, 80-96. <https://doi.org/10.1016/j.atmosres.2010.03.009>,](#)
600 [2010.](#)

601 Solomon, S., Rosenlof, K. H. and Portmann, R. W. et al.: Contributions of stratospheric water vapor to
602 decadal changes in the rate of global warming, Science, 327, 1219-1223,
603 <https://doi.org/10.1126/science.1182488>, 2010.

604 Sherwood, S. C. and Dessler, A. E.: A model for transport across the tropical tropopause, Journal of the
605 Atmospheric Sciences, 58, 765-779,
606 [https://doi.org/10.1175/1520-0469\(2001\)058<0765:AMFTAT>2.0.CO;2](https://doi.org/10.1175/1520-0469(2001)058<0765:AMFTAT>2.0.CO;2), 2001.

607 Smith, J. B., Wilmouth, D. M., and Bedka, K. M. et al.: A case study of convectively sourced water
608 vapor observed in the overworld stratosphere over the United States, Journal of Geophysical
609 Research: Atmospheres, 122(17), 9529-9554, <https://doi.org/10.1002/2017JD026831>, 2017.

610 Sun, N., Fu, Y., Zhong, L., Zhao, C. and Li, R.: The Impact of Convective Overshooting on the Thermal
611 Structure over the Tibetan Plateau in Summer Based on TRMM, COSMIC, Radiosonde, and
612 Reanalysis Data, Journal of Climate, 34, 8047-8063, <https://doi.org/10.1175/JCLI-D-20-0849.1>,
613 2021.

614 Sun, N., Fu, Y., Zhong, L. and Li, R.: Aerosol effects on the vertical structure of precipitation in East
615 China, npj Climate and Atmospheric Science, 5, 60, <https://doi.org/10.1038/s41612-022-00284-0>,
616 2022a.

617 Sun, N., Zhong, L., Zhao, C., Ma, M. and Fu, Y.: Temperature, water vapor and tropopause
618 characteristics over the Tibetan Plateau in summer based on the COSMIC, ERA-5 and IGRA datasets,
619 Atmospheric Research, 266, 105955, <https://doi.org/10.1016/j.atmosres.2021.105955>, 2022b.

带格式的: 字体: (中文) +中文正
文 (宋体), (中文) 中文(中国)

620 Sherwood, S. C., Horinouchi, T. and Zeleznik, H. A.: Convective impact on temperatures observed near
621 the tropical tropopause, *Journal of Atmospheric Sciences*, 60, 1847-1856,
622 [https://doi.org/10.1175/1520-0469\(2003\)060<1847:CIOTON>2.0.CO;2](https://doi.org/10.1175/1520-0469(2003)060<1847:CIOTON>2.0.CO;2), 2003.

623 Takahashi, H. and Luo, Z. J.: Characterizing tropical overshooting deep convection from joint analysis of
624 CloudSat and geostationary satellite observations, *Journal of Geophysical Research: Atmospheres*,
625 119, 112-121, <https://doi.org/10.1002/2013JD020972>, 2014.

626 Wang, X., Huang, Y., and Qu, Z. et al.: Convectively Transported Water Vapor Plumes in the
627 Midlatitude Lower Stratosphere, *Journal of Geophysical Research: Atmospheres*, 128(4),
628 e2022JD037699, <https://doi.org/10.1029/2022JD037699>, 2023.

629 Werner, F., Schwartz, M. J., and Livesey, N. J. et al.: Extreme outliers in lower stratospheric water
630 vapor over North America observed by MLS: Relation to overshooting convection diagnosed from
631 colocated Aqua - MODIS data, *Geophysical Research Letters*, 47(24), e2020GL090131,
632 <https://doi.org/10.1029/2020GL090131>, 2020.

633 World Meteorological Organization.: *Meteorology—A three - dimensional science: Second session of*
634 *the commission for aerology*, *WMO Bull*, 4, 134-138, 1957.

635 Xia, J.: *Research on climatic regionalization of China and characteristics of temperature, humidity and*
636 *wind in precipitation cloud*, University of Science and Technology of China, 2015.

637 Xu, W.: Thunderstorm climatologies and their relationships to total and extreme precipitation in China,
638 *Journal of Geophysical Research: Atmospheres*: 125, e2020JD033152,
639 <https://doi.org/10.1029/2020JD033152>, 2020.

640 Yuter, S. E. and Houze, R. A.: Three-dimensional kinematic and microphysical evolution of Florida
641 cumulonimbus. Part II: Frequency distributions of vertical velocity, reflectivity, and differential
642 reflectivity, *Monthly Weather Review*, 123(7), 1941-1963,
643 [https://doi.org/10.1175/1520-0493\(1995\)123<1941:TDKAME>2.0.CO;2](https://doi.org/10.1175/1520-0493(1995)123<1941:TDKAME>2.0.CO;2), 1995.

644 Zhang, A. and Fu, Y.: Life cycle effects on the vertical structure of precipitation in East China measured
645 by Himawari-8 and GPM DPR, *Monthly Weather Review*, 146, 2183-2199,
646 <https://doi.org/10.1175/MWR-D-18-0085.1>, 2018.

647 Zahn, A., Brenninkmeijer, C. A. M., and Van Velthoven, P. F. J.: Passenger aircraft project CARIBIC
648 1997–2002, Part I: the extratropical chemical tropopause, *Atmospheric Chemistry and Physics*
649 *Discussions*, 4(1), 1091-1117, <https://doi.org/10.5194/acpd-4-1091-2004>, 2004.

650

651 **Tables**

652 **Table1.** The sample number of total precipitation, convective precipitation, and convective overshooting over NC,
653 MEC, and SC.

654

Sample number (count, ct)	NC	MEC	SC
Total Precipitation	652489	546313	319127
Convective Precipitation	111903	137674	111900
Convective Overshooting	2394	582	296

655

656

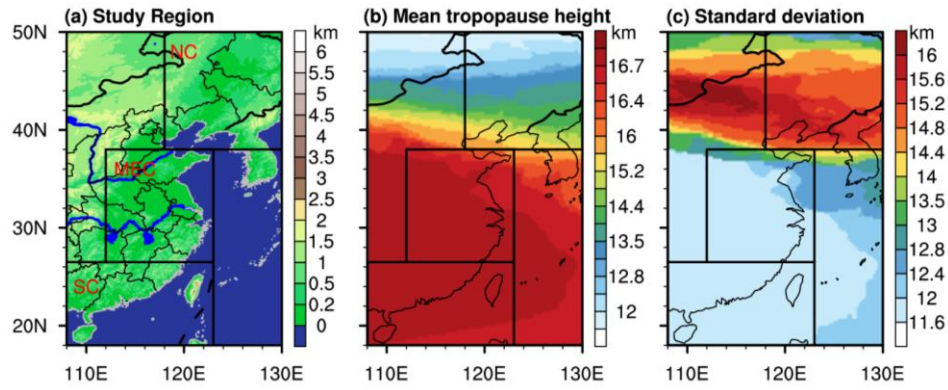
657

658

659

660 **Figures**

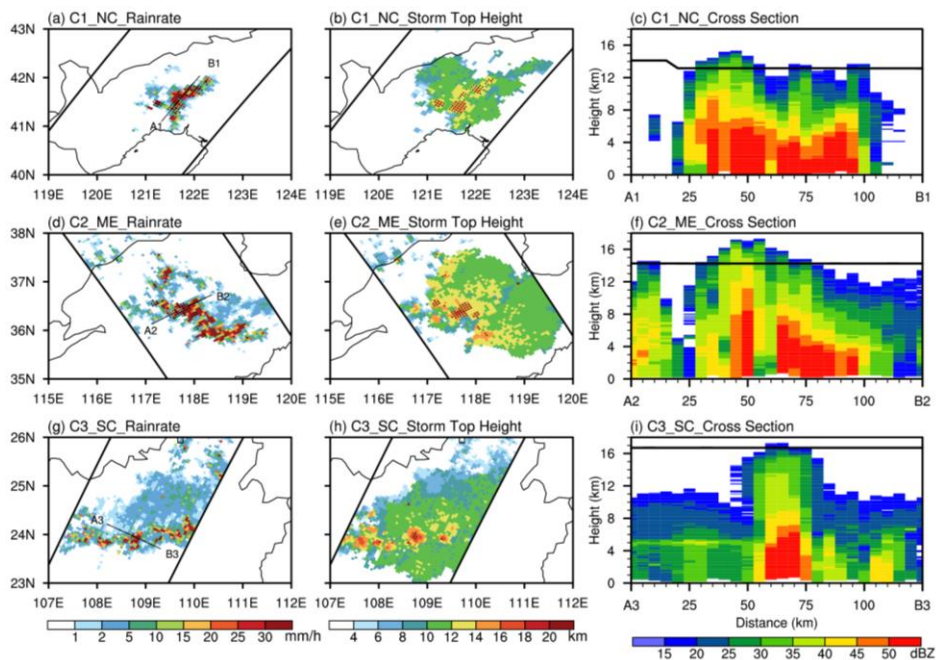
661



662

663 **Figure 1.** Study areas and their tropopause characteristics. **(a)** Regionalization of East China (Black boxes:
664 Divisions between NC, MEC and SC, and only the land surface is studied) and their terrain features. **(b)**
665 Climatological mean of tropopause height from 2014 to 2020 in summer (June, July and August). **(c)** Distribution
666 of standard deviation of tropopause height.

667



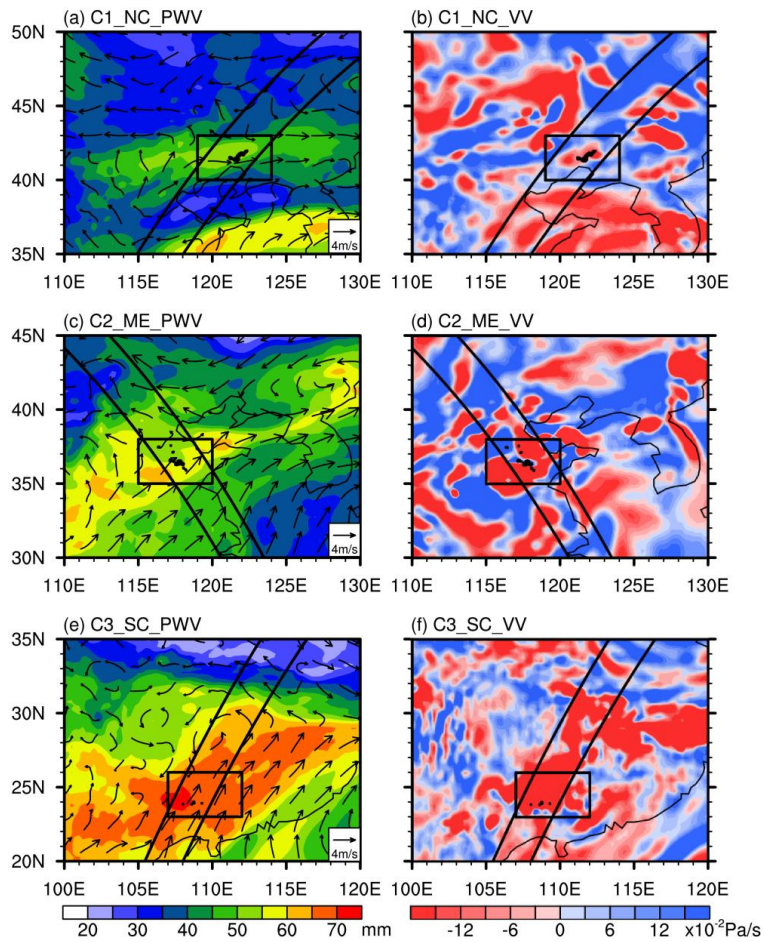
668

669

Figure 2. Precipitation characteristics of convective overshooting cases. **(a)** Distribution of rain rate of Case 1 (C1). **(b)** Distribution of storm top height of C1. **(c)** Radar reflectivity cross section along A1B1 and the black line show the tropopause height along A1B1. **(d)** Distribution of rain rate of C2. **(e)** Distribution of storm top height of C2. **(f)** Radar reflectivity cross section along A2B2. **(g)** Distribution of rain rate of C3. **(h)** Distribution of storm top height of C3. **(i)** Radar reflectivity cross section along A3B3.

674

675

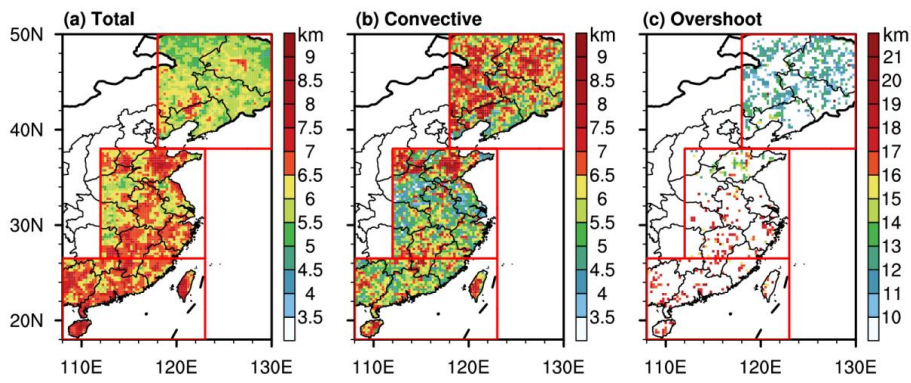


676

677

Figure 3. Characteristics of large scale circulation of convective overshooting cases. **(a)** Distribution of precipitable water vapor (PWV) and streamlines at 850 hPa of C1. The area where the case occurred is marked as big black boxes and the pixels in which convective overshooting occurs are marked as little black boxes. The black line is the GPM detection orbit. **(b)** Distribution of vertical velocity (VV) at 500 hPa of C1. **(c)** Distribution of PWV and streamlines of C2. **(d)** Distribution of VV of C2. **(e)** Distribution of PWV and streamlines of C3. **(f)** Distribution of VV of C3.

683



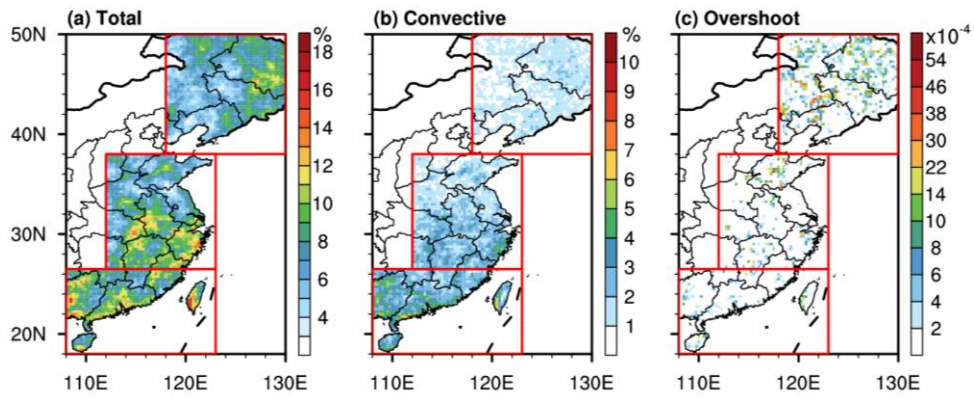
684

685 **Figure 4.** Geographical distribution of storm top height. (a) Distribution of storm top height for total precipitation.

686 (b) Distribution of storm top height for convective precipitation. (c) Distribution of storm top height for convective

687 overshooting.

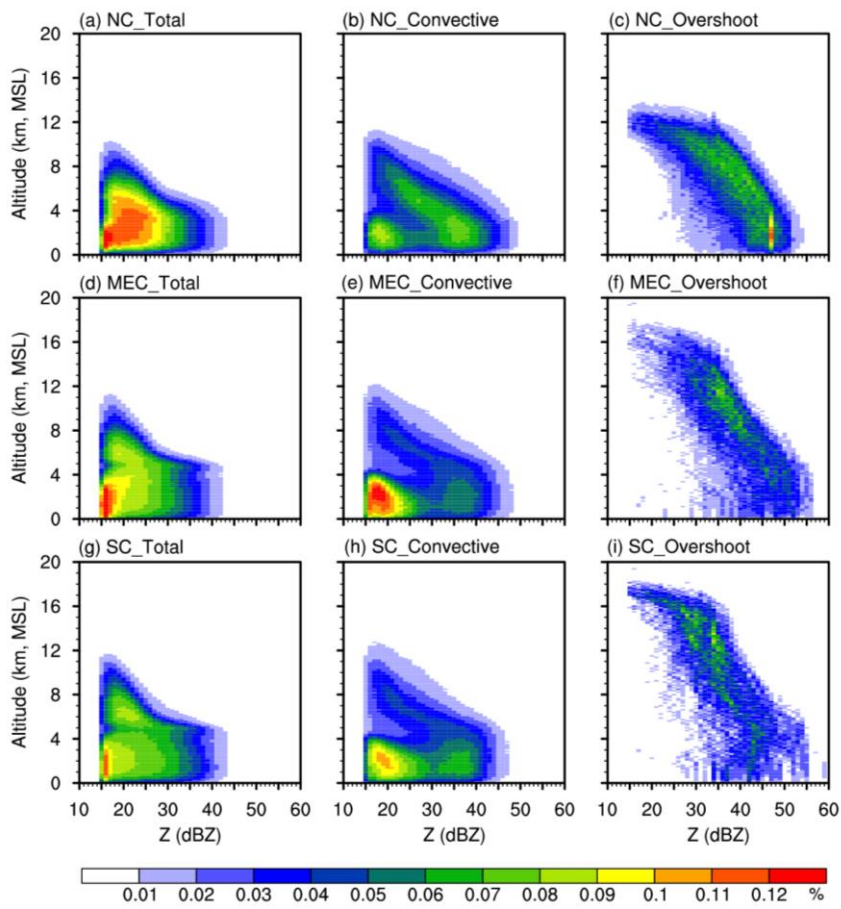
688



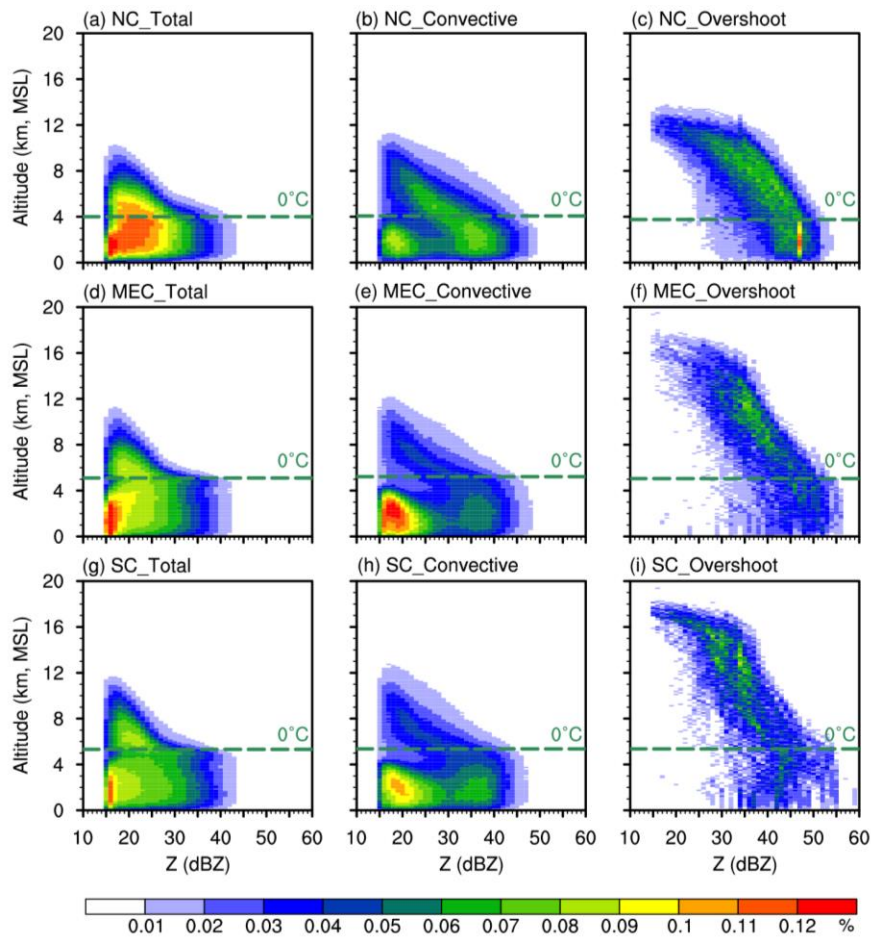
689

690 **Figure 5.** Precipitation frequency. **(a)** Frequency of total precipitation. **(b)** Frequency of convective precipitation.
 691 **(c)** Frequency of convective overshooting.

692

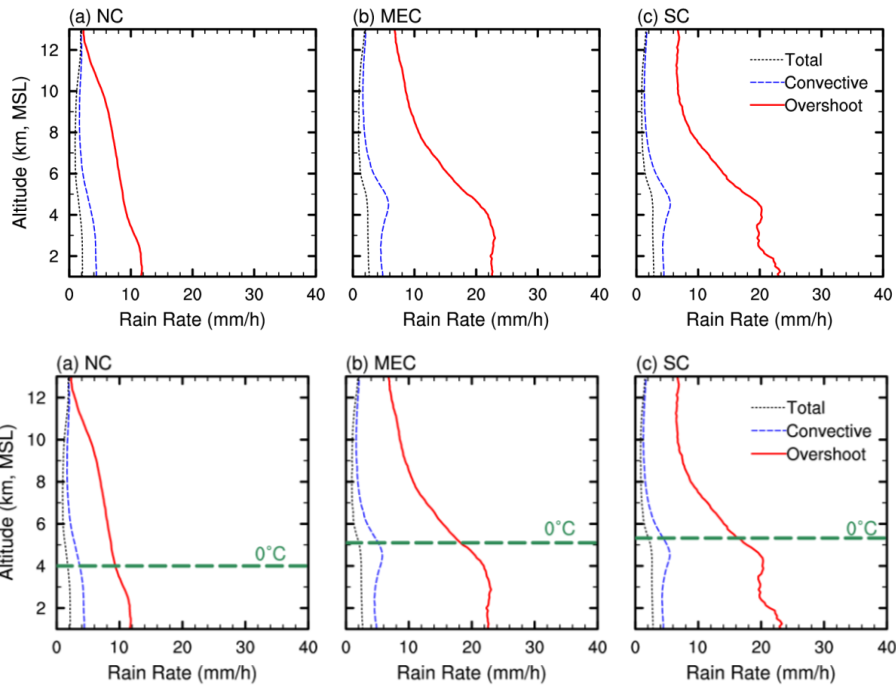


693



694

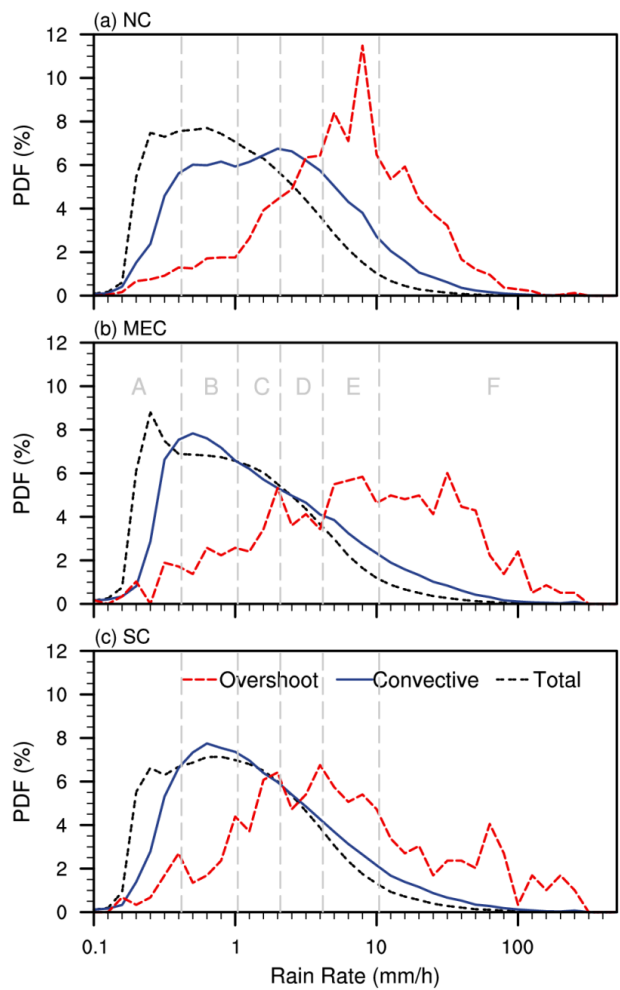
695 **Figure 6.** Contoured Frequency by Altitude Diagrams (CFADs) of radar reflectivity. **(a)** CFADs for total
 696 precipitation over NC. **(Green dotted line indicates the altitude of the freezing level).** **(b)** CFADs for convective
 697 precipitation over NC. **(c)** CFADs for convective overshooting over NC. **(d)** CFADs for total precipitation over
 698 MEC. **(e)** CFADs for convective precipitation over MEC. **(f)** CFADs for convective overshooting over MEC. **(g)**
 699 CFADs for total precipitation over SC. **(h)** CFADs for convective precipitation over SC. **(i)** CFADs for convective
 700 overshooting over SC.
 701



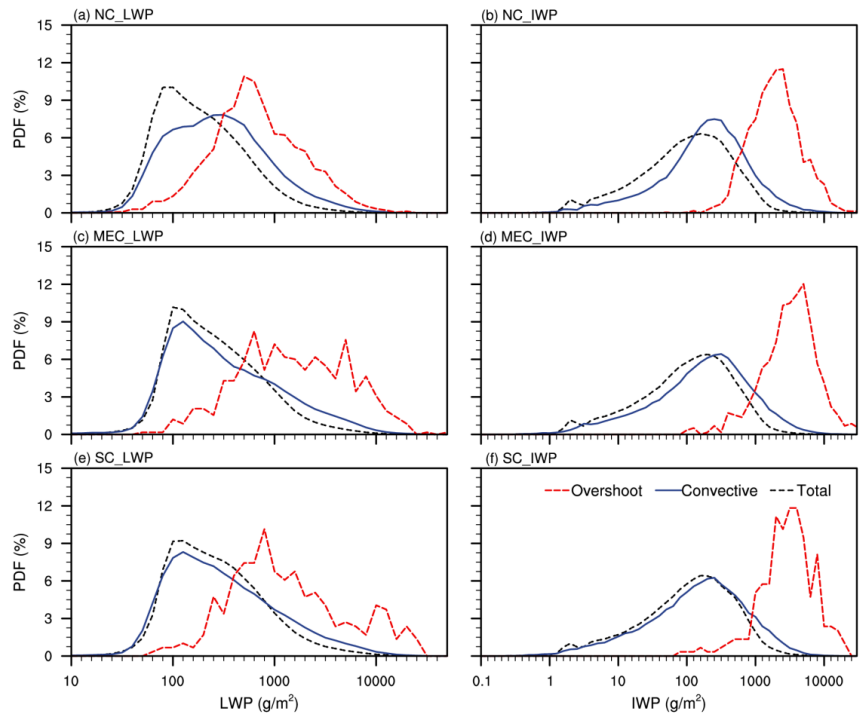
702

703

704 **Figure 7.** Rain rate profiles for total precipitation, convective precipitation and convective overshooting (Red lines
 705 are convective overshooting; Blue lines are the convective precipitation; Black lines are the total precipitation). (a)
 706 The rain rate profiles over NC (Green dotted line indicates the altitude of the freezing level). (b) The rain rate
 707 profiles over MEC. (c) The rain rate profiles over SC.
 708

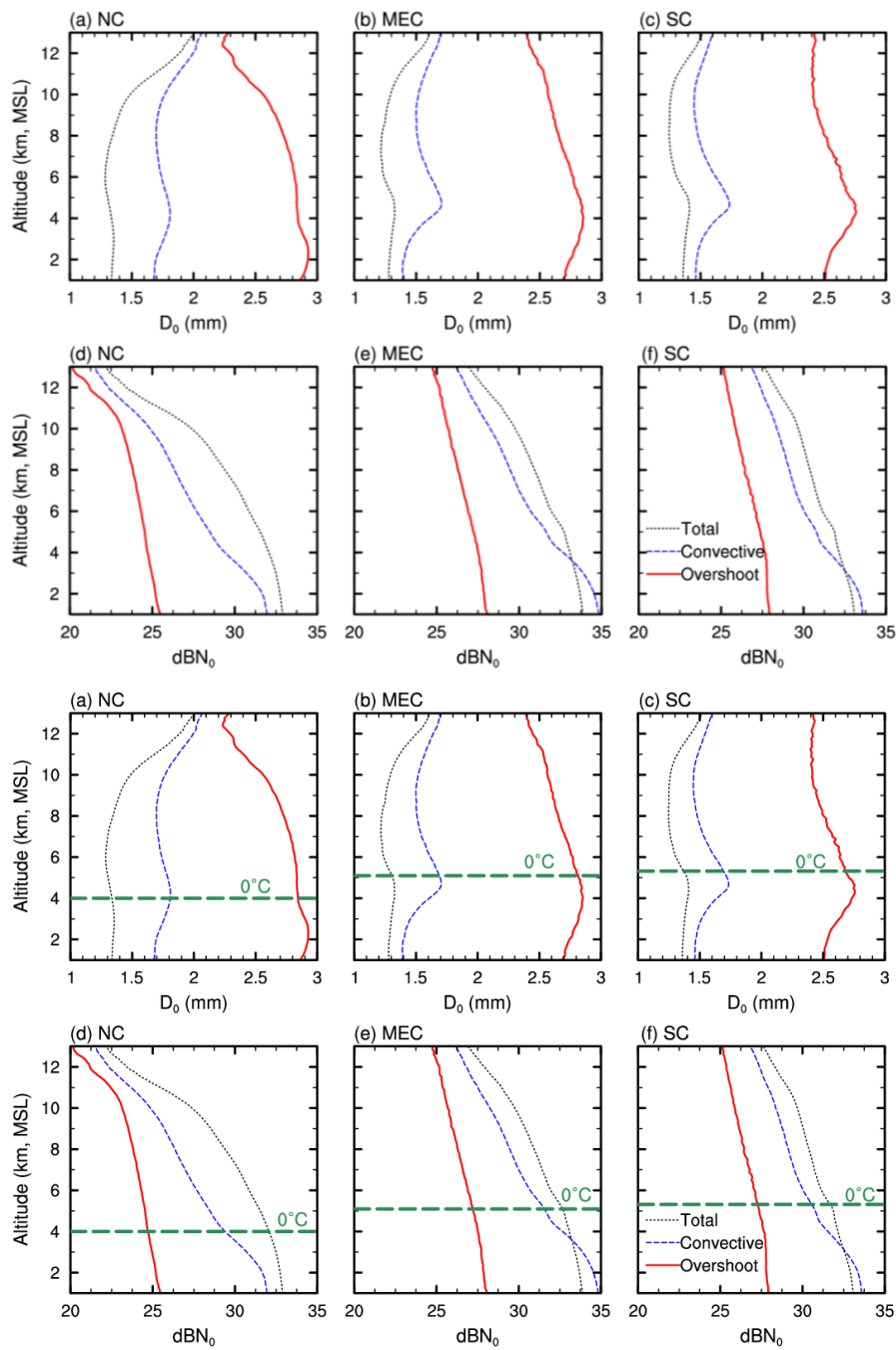


709
 710 **Figure 8.** Probability Density Function (PDF) of Near Surface Rain Rate (NSRR). (a) PDF of NSRR in NC. (b)
 711 PDF of NSRR in MEC. (c) PDF of NSRR in SC.



712
 713
 714
 715
 716

Figure 9. PDF of Liquid Water Path (LWP) and Ice Water Path (IWP). **(a)** PDF of LWP over NC. **(b)** PDF of IWP over NC. **(c)** PDF of LWP over MEC. **(d)** PDF of IWP over MEC. **(e)** PDF of LWP over SC. **(f)** PDF of IWP over SC.



717

718

719 **Figure 10.** The droplet concentration (dBN_0) and effective radius (D_0) profiles for total precipitation, convective
 720 precipitation and convective overshooting over NC, MEC and SC. (a) The dBN_0 profiles over NC (Green dotted
 721 line indicates the altitude of the freezing level). (b) The dBN_0 profiles over MEC. (c) The dBN_0 profiles over SC.
 722 (d) D_0 profiles over NC. (e) D_0 profiles over MEC. (f) D_0 profiles over SC.